# Photoexcitation circular dichroism in chiral molecules

S. Beaulieu [1,2], A. Comby[1], D. Descamps [1], B. Fabre [1], G. A. Garcia [3], R. Géneaux [4], A. G. Harvey [5], F. Légaré [2], Z. Mašín [5], L. Nahon [3], A. F. Ordonez [5,6], S. Petit [1], B. Pons[1]*, Y. Mairesse [1]*, O. Smirnova [5,6]* and V. Blanchet [1]

**Chiral effects appear in a wide variety of natural phenomena and are of fundamental importance in science, from particle physics to metamaterials. The standard technique of chiral discrimination—photoabsorption circular dichroism—relies on the magnetic properties of a chiral medium and yields an extremely weak chiral response. Here, we propose and demonstrate an orders of magnitude more sensitive type of circular dichroism in neutral molecules: photoexcitation circular dichroism. This technique does not rely on weak magnetic effects, but takes advantage of the coherent helical motion of bound electrons excited by ultrashort circularly polarized light. It results in an ultrafast chiral response and the efficient excitation of a macroscopic chiral density in an initially isotropic ensemble of randomly oriented chiral molecules. We probe this excitation using linearly polarized laser pulses, without the aid of further chiral interactions. Our time-resolved study of vibronic chiral dynamics opens a way to the efficient initiation, control and monitoring of chiral chemical change in neutral molecules at the level of electrons.**

The macro-world gives us many examples of chiral dynamics created by helical structures that convert rotations in a plane into translational motion orthogonal to it, from the Archimedes screw to plane propellers and household fans. In the micro-world, the electrons bound inside chiral molecules should develop a similar helical motion when excited by planar rotation of the electric field of circularly polarized light. Electronic excitation by circularly polarized light has been used to distinguish right-handed from left-handed molecules since 1896[1]. This technique, called photoabsorption circular dichroism (CD)[2], is based on the difference in the absorption of left- and right-circularly polarized light in chiral molecules and remains the go-to tool[3] for analysing properties of biological molecules, providing indispensable information on their structure, kinetics and thermodynamics, and interaction with their environment and with other molecules. However, it does not rely on the helical nature of bound electron currents, but uses the helical pitch of the light wave instead. This pitch, given by the wavelength of the absorbed light, $\lambda \gtrsim 2,500\,\text{Å}$ ($1\,\text{Å} = 10^{-8}\,\text{cm}$), is barely noticeable on the molecular scale of $\sim 1\,\text{Å}$, leading to very weak signals, three to four orders of magnitude less than the light absorption itself. Formally, the chiral-sensitive part of the light-induced excitation requires the excited electrons to respond to both the electric and the magnetic field of the light wave (see Fig. 1a).

Remarkably, in spite of extraordinary recent advances in developing new methods for chiral discrimination that do not rely on magnetic properties of the medium[4–15], none has relied on using the helical motion of bound electrons. Is it possible to excite and probe such motion without the help of magnetic field effects?

## Exciting chiral dynamics in bound states

A hallmark of helical motion of bound electrons is the appearance of an induced dipole orthogonal to the polarization plane of the exciting circular light. We first show that an ultrashort pulse creates such a dipole in a randomly oriented molecular ensemble. Let the electric field of the pulse, rotating in the $x$–$y$ plane, coherently excite two electronic states (Fig. 1b) of a chiral molecule. As shown in the Methods, the orientation-averaged induced dipole acquires the desired component along the light propagation direction $z$:

$$d_z^{\text{PXCD}} \propto \sigma[\mathbf{d}_{01} \times \mathbf{d}_{02}] \cdot \mathbf{d}_{12} \sin(\Delta E_{21} t) \qquad (1)$$

Here $\sigma = \pm 1$ is the light helicity, $\mathbf{d}_{01}$, $\mathbf{d}_{02}$ and $\mathbf{d}_{12}$ are the dipole transition vectors connecting the ground $|0\rangle$ and the two excited electronic states $|1\rangle$ and $|2\rangle$ (Fig. 1b), and $\Delta E_{21}$ is the energy spacing between the two excited states. For more than two states, equation (1) will contain the sum over all pairs of excited states $n,m$, leading to oscillations at all relevant frequencies $\Delta E_{nm}$. As a function of time, the induced dipole vector $\mathbf{d}^{\text{PXCD}}$ maps out a helix (Fig. 1b) and the $z$ component of the helical current is

$$j_z^{\text{PXCD}} \propto \sigma[\mathbf{d}_{01} \times \mathbf{d}_{02}] \cdot \mathbf{d}_{12} \Delta E_{21} \cos(\Delta E_{21} t) \qquad (2)$$

Both $d_z^{\text{PXCD}}$ and $j_z^{\text{PXCD}}$ are quintessential chiral observables (see, for example, refs [16,17]). Indeed, both are proportional to the light helicity $\sigma = \pm 1$ and to the triple product of three vectors $[\mathbf{d}_{01} \times \mathbf{d}_{02}] \cdot \mathbf{d}_{12}$. This triple product is a pseudo-scalar and as such presents a fundamental measure of chirality: it changes sign on reflection and thus has an opposite sign for left and right enantiomers. For randomly oriented non-chiral molecules $d_z^{\text{PXCD}} = j_z^{\text{PXCD}} = 0$.

Equations (1) and (2) lead to the following conclusions. First, the coherent excitation of electronic states leads to a charge displacement

[1]CELIA, Université de Bordeaux-CNRS-CEA, Talence, France. [2]Institut National de la Recherche Scientifique, Varennes, Quebec, Canada. [3]Synchrotron Soleil, l'orme des Merisiers, St Aubin, Gif sur Yvette, France. [4]LIDYL, Université Paris-Saclay-CNRS-CEA Saclay, Gif-sur-Yvette, France. [5]Max-Born-Institut, Berlin, Germany. [6]Technische Universität Berlin, Berlin, Germany. *e-mail: bernard.pons@u-bordeaux.fr; yann.mairesse@u-bordeaux.fr; Olga.Smirnova@mbi-berlin.de
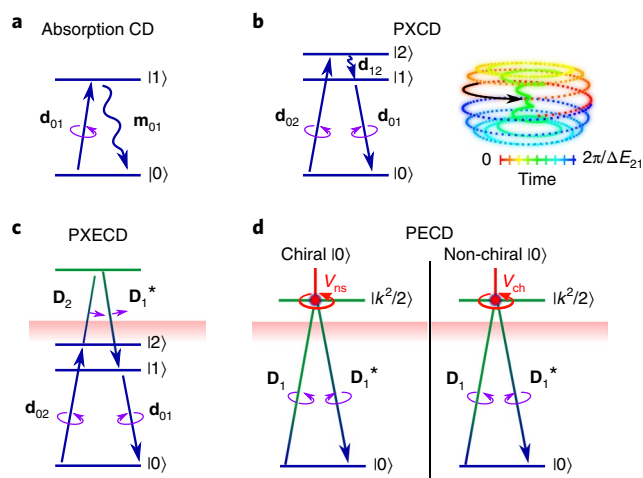
**Fig. 1 | Chiral discrimination schemes in randomly oriented molecular ensembles.** The complex conjugated diagrams, complementing those presented, are omitted. Down-arrows denote complex conjugation of driving fields. **a**, CD requires an electric dipole transition up, a magnetic dipole transition down and vice versa. **b**, PXCD (equation (1)) requires a coherent excitation of two states by an ultrashort circularly polarized pulse. The excitation dipole transition to state $|2\rangle$ is followed by a dipole transition to state $|1\rangle$ and a stimulated dipole transition to state $|0\rangle$. Inset: the induced dipole maps out a helix as a function of time. **c**, In PXECD (equation (3)), the two excited states $|1\rangle$ and $|2\rangle$ are connected by Raman-type transitions via the continuum, stimulated by a linearly polarized probe pulse. **d**, PECD requires a circularly polarized light and a photoelectron scattering in a chiral $V_{ch}$ (right panel) or non-spherically symmetric $V_{ns}$ potential (left panel). The red arrows indicate a torque (imparted on the emitted photoelectron) that survives the orientational averaging and induces the chiral response in PECD.

along the light propagation direction. Hence, a macroscopic dipole $d_z^{PXCD}$ and the corresponding chiral density are created in the excited states, with a chiral current oscillating out of phase for the two enantiomers. Second, photoexcitation circular dichroism (PXCD) requires no magnetic or quadrupole effects, and so, it is orders of magnitude stronger than standard photoabsorption CD. While photoabsorption CD exploits the helical pitch of the laser field in space, PXCD takes advantage of the subcycle rotation of the light field in time and is inherently ultrafast. PXCD arises only if the excitation dipoles $\mathbf{d}_{01}$, $\mathbf{d}_{02}$ are non-collinear: for the angle $\phi$ between the two transition dipoles, the PXCD (equations (1) and (2)) is proportional to $\sigma\sin(\phi)$. Since $\sigma = \pm 1$, $\sigma\sin(\phi) = \sin(\sigma\phi) = \sin(\sigma\omega\tau)$, where $\omega$ is the light frequency and $\tau = \phi/\omega$ is the time required by the light field to rotate by the angle $\phi$. PXCD vanishes if the coherence between excited states $|1\rangle$ and $|2\rangle$ is lost and it reflects the dynamical symmetry breaking in an isotropic medium. Our compact formulation of chiral response forms a common basis for understanding and linking together several different phenomena involving rotational[11] and bound–continuum dipole transitions[4] for chiral discrimination or dichroic phenomena[18]. The common requirement linking all of them is the non-collinearity of the excitation dipoles.

Is it possible to create PXCD from purely vibrational excitation of a chiral molecule? Theoretically, vibrational states within the same electronic state can also fulfil the PXCD condition as long as their dipoles are not collinear (see equations (1) and (2)). As shown in the Supplementary Information, this requires the breakdown of the Franck–Condon approximation (that is, a strong dependence of the electronic wavefunction on the position of the nuclei). In turn, this dependence leads to the appearance of electronic currents stimulated by the nuclear motion, which is triggered by the pump pulse.

Thus, vibrational PXCD is intertwined with the underlying chiral motion of electrons. The PXCD current can be induced with circularly polarized light either by direct coherent excitation of electronic states or by vibrational excitations with a strong coupling between electronic and vibrational degrees of freedom.

We now show that time-resolving PXCD does not require a chiral probe pulse. The coherence underlying PXCD allows a chiral object to 'interact with itself', albeit in a different quantum state, thus mimicking interaction with 'another chiral object' and removing any need for other chiral interactions during the probe step (Fig. 1). One such probe, termed photoexcitation-induced photoelectron circular dichroism (PXECD), is introduced below.

## Probing chiral dynamics in bound states

One way to probe the excited chiral density is to promote the chiral wavepacket to the electronic continuum using a linearly polarized pulse (Fig. 1c). As shown in the Methods, the standard photoionization observable, the photoelectron current averaged over molecular orientations, is:

$$J_z^{PXECD}(k) \propto \sigma[\mathbf{d}_{01} \times \mathbf{d}_{02}] \cdot \mathbf{D}_{12}^r(k)\sin(\Delta E_{21}\tau) + \sigma[\mathbf{d}_{01} \times \mathbf{d}_{02}] \cdot \mathbf{D}_{12}^i(k)\cos(\Delta E_{21}\tau) \quad (3)$$

with $J_x^{PXECD}(k) = J_y^{PXECD}(k) = 0$. Here $\tau$ is the pump–probe delay, $k$ is the photoelectron momentum and $\mathbf{D}_{12}(k) = \mathbf{D}_{12}^r(k) + i\mathbf{D}_{12}^i(k)$ is the Raman-type photoionization vector (see Fig. 1c and the Methods) that connects the excited bound states via the common continuum and plays the role of $\mathbf{d}_{12}$ of equations (1) and (2) (the real part of the Raman-type photoionization dipole is equal to zero due to the time-reversal symmetry of the setup).

The electron current in equation (3) contains a triple product. Just like the triple product $[\mathbf{d}_{01} \times \mathbf{d}_{02}] \cdot \mathbf{d}_{12}$ earlier, $[\mathbf{d}_{01} \times \mathbf{d}_{02}] \cdot \mathbf{D}_{12}^i$ will change sign on reflection. Thus, the electron current in equation (3) is a pseudo-scalar observable; it reverses its direction if the handedness $\sigma$ of the pump pulse or of the enantiomer is swapped, showing that PXECD is a genuine chiral effect. The chiral nature of the response arises only if the participating bound states are coherently excited. Once the coherence is lost, the chiral signal will also disappear.

Importantly, the state of the continuum does not need to be chiral, as it only provides a link between the two chiral bound states $|1\rangle$ and $|2\rangle$ (Fig. 1c). $J_z^{PXECD}(k)$ remains chiral even for a plane-wave continuum (see the Methods); $\mathbf{D}_{12}(k)$ has only an imaginary component:

$$J_{z,PW}^{PXECD}(k) \propto -\sigma[\mathbf{d}_{01} \times \mathbf{d}_{02}] \cdot \mathbf{D}_{12}^{i,PW}(k)\cos(\Delta E_{21}\tau) \quad (4)$$

Note also that the total PXECD photoelectron current $J_{tot}^{PXECD} \equiv \int J_{z,PW}^{PXECD}(k)dk$ measures the chiral current excited in bound states $j_z^{PXCD}$ (equation (2)) (that is, $J_{tot}^{PXECD} \propto j_z^{PXCD}$ (see Supplementary Information)) because $-1/2 \int \mathbf{D}_{12}^{i,PW}(k)dk \equiv \Delta E_{12}\mathbf{d}_{12}$. In particular, for $\Delta E_{12} = 0$ both the PXCD bound and the PXECD continuum currents vanish.

One might think that partial alignment of the excited molecular ensemble could already be fully responsible for enabling non-chiral probes of chiral dynamics. However, it is not true in our case. Indeed, the effect of alignment persists for a single excited electronic state and for the two excited electronic states with collinear dipoles, but in both cases it leads to zero PXECD current. Finally, removing the effect of partial alignment shows that the PXECD current remains chiral for every $k$ (see Methods).

Probing the created chiral excitation using photoelectron imaging with linearly polarized light constitutes yet another new

phenomenon. The PXECD is reminiscent of photoelectron circular dichroism (PECD)[4–6,13–15,19], which arises when circularly polarized light is used to photoionize a chiral molecule. However, there is a fundamental difference. PECD can exist only if the molecular potential felt by the emitted electron is either chiral[4] or, at least, non-spherically symmetric[20] (both effects quickly disappearing for photoelectron energies above 10 to 20 eV), while the initial orbital may or may not be chiral at all[21] (see Fig. 1d and Supplementary Information).

In contrast to PECD, PXECD requires neither chiral light, nor chiral or asymmetric scattering of the photoelectron. It can be observed both at low and high photoelectron energies. If one chooses to observe it at low energies, the chiral continuum may affect imaging of the bound chiral current. Nevertheless, if the bound dynamics is excited but the PXCD helical current (electronic or vibronic) is absent (that is, the excited dynamics is not chiral), its measurement with linear light will yield zero chiral response (unless the 'up–down' symmetry of the continuum states with respect to the plane determined by the excitation dipoles is different from that of the excited Rydberg wavepacket). Thus, if the experiment detects a time-dependent chiral signal, it demonstrates the presence of bound chiral dynamics. This contrasts PXECD with time-resolved PECD measurement, which uses a circularly polarized probe: it can yield non-zero chiral response even if the excited dynamics is not chiral.

Since time-resolved PXECD does not require the technically challenging use of ultrashort circularly polarized extreme ultraviolet pulses[22–26], it opens unique perspectives for ultrafast chiral-sensitive measurements using readily available ultrashort linearly polarized extreme ultraviolet light.

We shall now confirm both numerically and experimentally that our scheme provides a sensitive time-resolved probe of chiral molecular dynamics in bound states.

### Theoretical analysis in fenchone

To quantify the PXECD effect, we performed quantum mechanical calculations on fenchone molecules (see Supplementary Information). First, we simulated the PXCD phenomenon and calculated the excitation of the $s$ and $p$ manifolds of Rydberg states in fenchone by a circular pump pulse. On averaging over a random initial orientation of molecules, the resulting electron density of the Rydberg wavepacket is asymmetric in the $z$ direction in the

momentum space. The asymmetry reverses if the helicity of the pump pulse or the handedness of the molecule is reversed. The strength of the PXCD can be quantified by the magnitude of the chiral component of the excited electron density. It is obtained by subtracting the momentum space density $D$ obtained with right (R) and left (L) circularly polarized light: PXCD $= 2(D(L) - D(R))/(D(L) + D(R))$. The calculated PXCD reaches very high values (35%, Fig. 2a). The asymmetry of the charge distribution describes a macroscopic dipole moment $d_z^{PXCD}$ that reaches 3 debye (Fig. 2b) and oscillates at frequencies determined by the energy differences between the states forming the electronic wavepacket. The pump–probe PXECD signal, calculated as $(D(L) - D(R))$ and normalized to the maximum of $(D(L) + D(R))/2$, reveals temporal oscillations (Fig. 2c) and 6% asymmetry, owing to the short duration of the probe pulse (36 fs full-width at half-maximum (FWHM) in intensity). The asymmetry scales with the probe bandwidth $\Delta W_{FWHM}$ as $e^{-[\Delta E_{12}\sqrt{\ln 2}/\Delta W_{FWHM}]^2}$ (see Supplementary Information), decreasing for longer probe pulses such as used in the experiment.

### Observation of PXECD in fenchone

In our experiment, a circularly polarized femtosecond pump pulse at 201 nm (6.17 eV photon energy, 80 meV at $1/e^2$ electric field bandwidth) photoexcites enantiopure fenchone molecules from a supersonic gas jet in the interaction zone of a velocity map imaging spectrometer. The molecules are excited to Rydberg bands through single-photon absorption (Fig. 3a, see Supplementary Information). A time-delayed, linearly polarized probe pulse at 405 nm (3.1 eV photon energy, 85 meV at $1/e^2$ of the electric field bandwidth) induces one-photon ionization of the excited molecules. The cross-correlation of the pump and the probe pulses is 170 fs. The photoelectrons are accelerated and projected by an electrostatic lens onto a set of dual microchannel plates and imaged by a phosphor screen and a CCD (charge-coupled device) camera. The (L) and (R) photoelectron images are recorded alternatively using left and right circularly polarized pump pulses respectively. The difference (L − R) and sum (L + R) of these two images are fitted by a linear combination of Legendre polynomials using a least-square fitting algorithm (p-Basex, see Supplementary Information for details). The PXECD is given by the (L − R) image while the (L + R) image reflects the angle-resolved photoelectron spectrum (PES). These
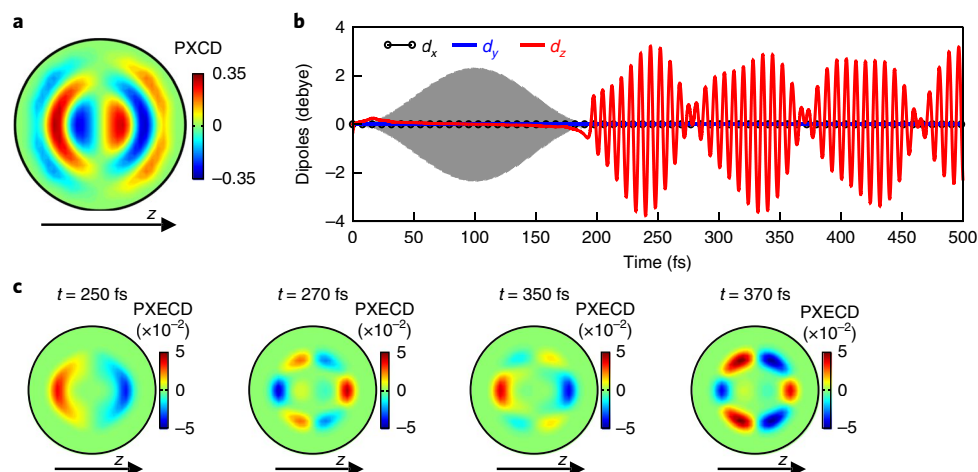


**Fig. 2 | Theoretical analysis of the electron chiral dynamics in (1S)-(+)-fenchone. a**, The momentum-space electron density underlying PXCD. The asymmetry resulting from the chirality of the electron density is formed along the light propagation direction $z$. **b**, Temporal evolution of the $x$, $y$ and $z$ components of the macroscopic dipole associated with the (3s,3p) Rydberg wavepacket created by the pump pulse (the shaded area). Only the $z$ component, along the direction of propagation of the pump and probe pulses, survives orientational averaging. **c**, Momentum-space PXECD signals at various pump–probe delays $t$ calculated with a probe duration of 36 fs (full-width at half-maximum in intensity).

two images shown in Fig. 3b for a 200 fs pump–probe delay are both normalized by the peak of the $(L+R)/2$ image. As expected, a significant amplitude of the PXECD image is observed, reaching 2%. The asymmetry reverses for the other enantiomer of $(1S)$-$(+)$-fenchone (see Supplementary Fig. 4), proving the enantio-sensitivity of the effect, originating from the pseudo-scalar nature of the PXECD current (see equation (3)). The forward–backward asymmetry (that is, the normalized difference of photoelectron counts between the forward and the backward hemispheres relative to the $z$ axis) is $-1.86\% \pm 0.14\%$ for $(1S)$-$(+)$-fenchone and $+1.68\% \pm 0.34\%$ for $(1R)$-$(-)$-fenchone, at 700 fs delay.

The photoelectron spectrum, obtained from the first even term of the Legendre decomposition (see Supplementary Information), contains a single broad component in energy, corresponding to ionization from the outermost orbital (vertical ionization potential 8.72 eV). This component does not shift in energy with the pump–probe delay (Fig. 4b) and decays exponentially in 3.3 ps, reflecting a simple vibronic relaxation of the Rydberg population onto lower states that cannot be photoionized by one probe photon alone. The temporal evolution of the PXECD image shows much richer spectroscopic features, which can be analysed by decomposing it in odd Legendre polynomials (Fig. 4a). We note that a sum of first- and third-order Legendre polynomials, with coefficients $\alpha$ and $\alpha'$, is enough to fit the PXECD images. Both coefficients maximize around ~50 meV below the maximum of the PES. The PXECD

**Fig. 4 | Time-resolved PXECD in fenchone and camphor. a**, Legendre polynomial decomposition of the PXECD image for $(1S)$-$(+)$-fenchone at 200 fs pump–probe delay. The $\alpha, \alpha'$ coefficients, already normalized to the maximum value of the $(L+R)/2$ image, are multiplied by their associated Legendre polynomials $P_l(\theta)$: $P_1 = \cos(\theta)$, $P_3 = ((5/2)\cos^3(\theta) - (3/2)\cos(\theta))$ to reconstruct the PXECD image. **b**, Evolution of the PES and PXECD coefficients as a function of the pump–probe delay and the photoelectron kinetic energy, in $(1S)$-$(+)$-fenchone with a 201 nm pump, and in $(1R)$-$(+)$-camphor with a 202 nm pump or with a 200 nm pump. The black dotted lines represent the kinetic energy of the photoelectron corresponding to the maximum of PES. The decay times of the main PES component are $3.28 \pm 0.05$ and $2.36 \pm 0.07$ ps for fenchone and camphor, respectively.
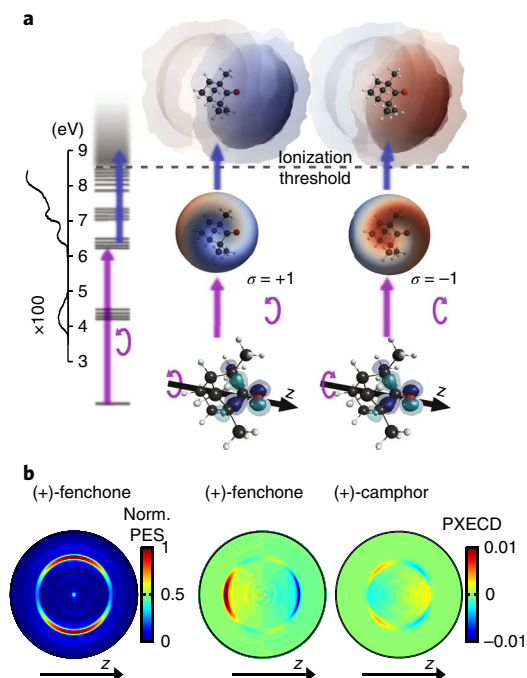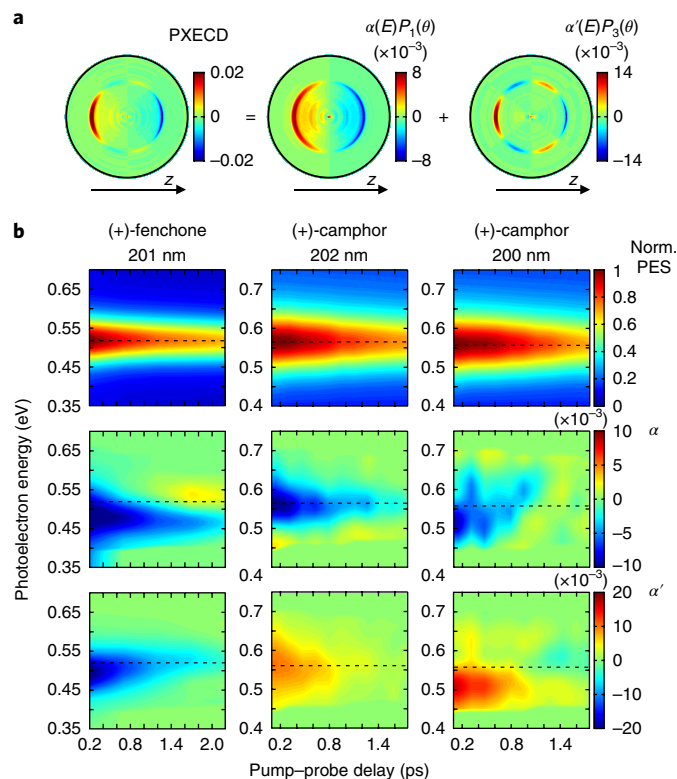
**Fig. 3 | PXECD in fenchone molecules. a**, Artist's impression of PXECD. The absorption of a circularly polarized femtosecond pulse at 201 nm with helicity $\sigma = \pm 1$ promotes an electron from the highest occupied molecular orbital to Rydberg bands, creating a chiral vibronic wavepacket. A linearly polarized femtosecond probe pulse at 405 nm photoionizes the molecule, revealing the chiral asymmetry of the Rydberg wavepacket in the angular distribution of the photoelectrons. The absorption spectrum of fenchone is adapted from a previous study[39]. **b**, Experimental images of $(L+R)$ image (PES) and $(L-R)$ image (PXECD) at the 200 fs pump–probe delay for $(1S)$-$(+)$-fenchone and $(1R)$-$(+)$-camphor. The characteristic forward–backward asymmetry of the photoelectron is observed along the light propagation direction $z$. The PXECD image of $(1R)$-$(-)$-fenchone is shown in Supplementary Fig. 4.

signal (Fig. 4b) can be decomposed into two components: below and above the maximum of the PES. The low-energy component of $\alpha$ undergoes a rather smooth decay. On the contrary, its high-energy component decays very quickly and even changes sign around 1 ps. For $\alpha'$, the behaviour is opposite; that is, the high-energy component shows much slower dynamics than the low-energy part. Such time-dependent and electron-energy-dependent behaviour is characteristic of internal vibrational torsional motion and may indicate the change of the chiral structure of the molecule induced by such motion. Indeed, the electronic excitation of the molecules is expected to be accompanied by a significant vibrational excitation, since the equilibrium geometries of Rydberg states are quite different from that of the ground state. The molecules will tend to relax towards the equilibrium geometry of the Rydberg states, and oscillate around it. Figure 5 illustrates the influence of this change of molecular geometry on the calculated PXECD signal. Even small bond length changes ($\leq 7\%$) lead to significant modification of the PXECD signal. This demonstrates the remarkable sensitivity of PXECD to molecular vibrations, which follow the electronic excitation. The ensuing vibrational dynamics will inevitably blur the purely electronic oscillations shown in Fig. 2c. At 4 ps (not shown), the PXECD completely vanishes while

the Rydberg population is still 30% of its initial value. This result unambiguously reflects the loss of wavepacket coherence that halts chiral dynamics in our experiment.

### Observation of PXECD in camphor

According to numerical simulations (see Supplementary Information), the coherence between the two Rydberg bands could eventuate in fenchone. However, the s and p Rydberg bands of camphor are upshifted by an additional several tens of millielectronvolts compared with fenchone, preventing direct excitation of the p states by the pump pulse. The experiment still reveals a strong PXECD signal, indicating that a chiral vibronic wavepacket has been created in camphor. Both PXCD and PXECD are highly molecular specific (Fig. 3b): the PXECD images from the two isomers (camphor and fenchone) are drastically different. The $\alpha'$ coefficients in camphor and fenchone are of opposite sign as seen in multiphoton[27] and one-photon PECD[14]. In our experiment, this could be a consequence of PXECD sensitivity to isomerism (see Fig. 5 to gauge the sensitivity to nuclear configuration), but it might also be a signature of the different nature of the excited chiral electronic currents in fenchone and camphor. Changing the excitation wavelength from 202 nm to 200 nm does not affect the monoexponential decay of the PES. In contrast, a strong change is observed in the PXECD: the $\alpha'$ magnitude is almost twice as large and it is shifted in energy towards the red wing of the photoelectron spectrum. The drastic change observed in the PXECD signal in camphor once the pump photon energy is increased by only 60 meV illustrates the extreme sensitivity of this measurement to the excited vibrational dynamics.

### Conclusions and outlook

The ensemble-averaged chiral charge density arising in PXCD implies asymmetry in the charge distribution along the light propagation direction, induced by the planar rotation of light polarization but not by light's helical structure. Depending on the medium density, this could lead to a very large coherently oscillating macroscopic

dipole. The phase of this oscillation is opposite for two enantiomers, leading to macroscopic enantio-sensitive effects. The existence of the enantio-sensitive macroscopic dipole, which also occurs for purely rotational excitation[11,28], opens a way to laser-driven separation of enantiomers in isotropic racemic mixtures in the gas phase.

The application of a linearly polarized X-ray probe in PXECD would enable genuine probing of ultrafast chiral bound dynamics, since PXECD does not require chiral interaction in the continuum, which becomes negligible for sufficiently high-energy electrons. Therefore, the PXCD phenomenon opens the way to direct visualization of chiral electronic density using time-resolved X-ray diffraction imaging, both in the gas and condensed phase. Intense ultrafast sources of X-ray radiation, such as free-electron lasers, combined with measurements sensitive to valence-shell dynamics in the gas phase[29] should lead to few-femtosecond time resolution of chiral charge dynamics. Finally, PXCD could be used to drive molecular reactions in chiral systems in a stereo-specific way, by imprinting a chiral torque via the helicity of the exciting circularly polarized pulse. The ultrafast charge dynamics triggered by coherent electronic excitation is reminiscent of ultrafast charge migration triggered by photoionization[30–36] recently observed[37] and speculated to underlie charge-directed reactivity in cations[38]. Chiral electron stereo-dynamics in neutral molecules may open similar opportunities for controlling charge and energy flow in molecules at the level of electrons, offering new perspectives for such intriguing problems as asymmetric synthesis, a major challenge in stereochemistry.

### Methods

Methods, including statements of data availability and any associated accession codes and references, are available at https://doi.org/10.1038/s41567-017-0038-z.

### References

1. Cotton, A. Recherches sur l'absorption et la dispersion de la lumière par les milieux doués du pouvoir rotatoire. *J. Phys. Theor. Appl.* **5**, 237–244 (1896).
2. Barron, L. D. *Molecular Light Scattering and Optical Activity.* 2nd edn (Cambridge University Press: Cambridge, 2004).
3. Berova, N, Nakanishi, K. & Woody, R. *Circular Dichroism: Principles and Applications.* 2nd edn, (Wiley: New York, NY, 2000).
4. Ritchie, B. Theory of the angular distribution of photoelectrons ejected from optically active molecules and molecular negative ions. *Phys. Rev. A* **13**, 1411–1415 (1976).
5. Powis, I. Photoelectron circular dichroism of the randomly oriented chiral molecules glyceraldehyde and lactic acid. *J. Chem. Phys.* **112**, 301–310 (2000).
6. Böwering, N. et al. Asymmetry in photoelectron emission from chiral molecules induced by circularly polarized light. *Phys. Rev. Lett.* **86**, 1187–1190 (2001).
7. Lux, C. et al. Circular dichroism in the photoelectron angular distributions of camphor and fenchone from multiphoton ionization with femtosecond laser pulses. *Angew. Chem. Int. Ed.* **51**, 5001–5005 (2012).
8. Lehmann, C. S., Ram, N. B., Powis, I. & Janssen, M. H. M. Imaging photoelectron circular dichroism of chiral molecules by femtosecond multiphoton coincidence detection. *J. Chem. Phys.* **139**, 234–307 (2013).
9. Pitzer, M. et al. Direct determination of absolute molecular stereochemistry in gas phase by coulomb explosion imaging. *Science* **341**, 1096–1100 (2013).
10. Herwig, P. et al. Imaging the absolute configuration of a chiral epoxide in the gas phase. *Science* **342**, 1084–1086 (2013).
11. Patterson, D., Schnell, M. & Doyle, J. M. Enantiomer-specific detection of chiral molecules via microwave spectroscopy. *Nature* **497**, 475–477 (2013).
12. Yachmenev, A. & Yurchenko, S. N. Detecting chirality in molecules by linearly polarized laser fields. *Phys. Rev. Lett.* **117**, 033001 (2016).
13. Comby, A. et al. Relaxation dynamics in photoexcited chiral molecules studied by time-resolved photoelectron circular dichroism: toward chiral femtochemistry. *J. Phys. Chem. Lett.* **7**, 4514–4519 (2016).
14. Nahon, L., Garcia, G. A. & Powis, I. Valence shell one-photon photoelectron circular dichroism in chiral systems. *J. Electron Spectrosc. Relat. Phenom.* **204**, 322–334 (2015).
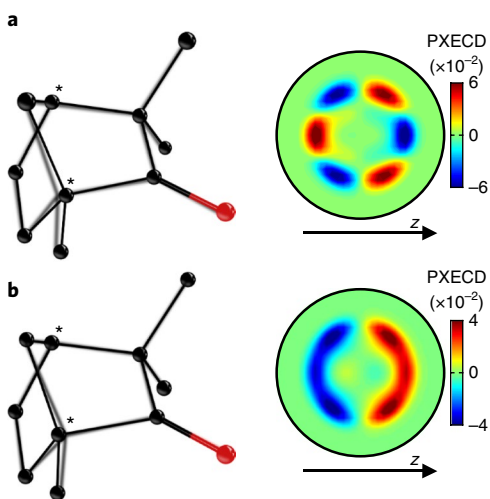
**Fig. 5 | Sensitivity of PXECD in (1S)-(+)-fenchone to the evolution of the chiral molecular structure. a,** The equilibrium geometries of the ground (dark) and 3 s (shadowed) electronic states, and the PXECD signal computed at $t = 370$ fs using the ground-state geometry for both the pump excitation and the probe ionization. **b,** The representation of the geometries are exchanged and the PXECD is now calculated for a probe ionization that occurs from a vibronic wavepacket localized at the 3 s equilibrium geometry. The PXECD image is averaged over random molecular orientations and calculated with a 36 fs duration of the probe pulse.

15. Nahon, L. et al. Determination of accurate electron chiral asymmetries in fenchone and camphor in the VUV range: sensitivity to isomerism and enantiomeric purity. *Phys. Chem. Chem. Phys.* **18**, 12696–12706 (2016).

16. Barron, L. D. True and false chirality and absolute asymmetric synthesis. *J. Am. Chem. Soc.* **108**, 5539–5542 (1986).

17. Tang, Y. & Cohen, A. E. Optical chirality and its interaction with matter. *Phys. Rev. Lett.* **104**, 163901 (2010).

18. Cherepkov, N. A. & Raşeev, G. Linear dichroism in the angular distribution of photoelectrons. *J. Chem. Phys.* **103**, 8238–8246 (1995).

19. Garcia, G. A., Nahon, L., Daly, S. & Powis, I. Vibrationally induced inversion of photoelectron forward–backward asymmetry in chiral molecule photoionization by circularly polarized light. *Nat. Commun.* **4**, 2132 (2013).

20. Stener, M., Di Tommaso, D., Fronzoni, G., Decleva, P. & Powis, I. Theoretical study on the circular dichroism in core and valence photoelectron angular distributions of camphor enantiomers. *J. Chem. Phys.* **124**, 024326 (2006).

21. Ulrich, V. et al. Giant chiral asymmetry in the C1s core level photoemission from randomly oriented fenchone enantiomers. *J. Phys. Chem. A* **112**, 3544–3549 (2008).

22. Wang, T. et al. Femtosecond single-shot imaging of nanoscale ferromagnetic order in Co/Pd multilayers using resonant x-ray holography. *Phys. Rev. Lett.* **108**, 267403 (2012).

23. Spezzani, C. et al. Coherent light with tunable polarization from single-pass free-electron lasers. *Phys. Rev. Lett.* **107**, 084801 (2011).

24. Allaria, E. et al. Highly coherent and stable pulses from the FERMI seeded free-electron laser in the extreme ultraviolet. *Nat. Photon.* **6**, 699–704 (2012).

25. Fleischer, A., Kfir, O., Diskin, T., Sidorenko, P. & Cohen, O. Spin angular momentum and tunable polarization in high-harmonic generation. *Nat. Photon.* **8**, 543–549 (2014).

26. Ferré, A. et al. A table-top ultrashort light source in the extreme ultraviolet for circular dichroism experiments. *Nat. Photon.* **9**, 93–98 (2015).

27. Lux, C., Wollenhaupt, M., Sarpe, C. & Baumert, T. Photoelectron circular dichroism of bicyclic ketones from multiphoton ionization with femtosecond laser pulses. *ChemPhysChem* **16**, 115–137 (2015).

28. Eibenberger, S., Doyle, J. & Patterson, D. Enantiomer-specific state transfer of chiral molecules. *Phys. Rev. Lett.* **118**, 123002 (2017).

29. Bredtmann, T., Ivanov, M. & Dixit, G. X-ray imaging of chemically active valence electrons during a pericyclic reaction. *Nat. Commun.* **5**, 5589 (2014).

30. Lunnemann, S., Kuleff, A. I. & Cederbaum, L. S. Ultrafast charge migration in 2-phenylethyl-N,N-dimethylamine. *Chem. Phys. Lett.* **450**, 232–235 (2008).

31. Breidbach, J. & Cederbaum, L. S. Universal attosecond response to the removal of an electron. *Phys. Rev. Lett.* **94**, 033901 (2005).

32. Remacle, F. & Levine, R. D. An electronic time scale in chemistry. *Proc. Natl Acad. Sci. USA* **103**, 6793–6798 (2006).

33. Kuleff, A. I. & Cederbaum, L. S. Charge migration in different conformers of glycine: The role of nuclear geometry. *Chem. Phys.* **338**, 320–328 (2007).

34. Lepine, F. Ivanov, M. Y. & Vrakking, M. J. J. Attosecond molecular dynamics: Fact or fiction? *Nat. Photon.* **8**, 195–204 (2014).

35. Leone, S. R. et al. What will it take to observe processes in 'real time'? *Nat. Photon.* **8**, 162–166 (2014).

36. Kuleff, A. I. & Cederbaum, L. S. Ultrafast correlation-driven electron dynamics. *J. Phys. B* **47**, 124002 (2014).

37. Calegari, F. et al. Ultrafast electron dynamics in phenylalanine initiated by attosecond pulses. *Science* **346**, 336–339 (2014).

38. Weinkauf, R., Schlag, E. W., Martinez, T. J. & Levine, R. D. Nonstationary electronic states and site-selective reactivity. *J. Phys. Chem. A* **101**, 7702–7710 (1997).

39. Pulm, F., Schramm, J., Hormes, J., Grimme, S. & Peyerimhoff, S. D. Theoretical and experimental investigations of the electronic circular dichroism and absorption spectra of bicyclic ketones. *Chem. Phys.* **224**, 143–155 (1997).

## Author contributions

S.B., A.C., R.G., Y.M. and V.B., performed the experiment. D.D. and S.P. operated the laser system. S.B., A.C., B.F., G.A.G., L.N., B.P., Y.M. and V.B. analysed the data. B.F. and B.P. performed the molecular geometry and dynamical calculations. A.G.H., A.F.O., Z.M. and O.S. developed the analytical theory, A.F.O. and O.S. derived triple-product chirality measures for PXCD and PXECD and analysed their connection and properties. S.B. wrote the first version of the manuscript; all authors contributed to writing the manuscript.

## Competing interests

The authors declare no competing financial interests.

## Additional information

**Supplementary information** is available for this paper at https://doi.org/10.1038/s41567-017-0038-z.

**Reprints and permissions information** is available at www.nature.com/reprints.

**Correspondence and requests for materials** should be addressed to B.P. or Y.M. or O.S.

**Publisher's note**: Springer Nature remains neutral with regard to jurisdictional claims in published maps and institutional affiliations.

## Methods

Full details of the analysis of photoexcitation circular dichroism (PXCD) and its probing are given in the Supplementary Information. Here we present its key steps.

**Exciting chiral currents.** To derive equations (1) and (2) for the $z$ components of the induced dipole and current, we use standard time-dependent perturbation theory, assuming two excited states $i=1,2$ coupled to the ground state. The pump field in the laboratory frame (superscript L) is:

$$\mathbf{E}^L(t) = \frac{1}{\sqrt{2}} F(t)\hat{\varepsilon}_\sigma^L e^{-i(\omega t + \delta)} + \text{c.c.} \tag{5}$$

where $\omega$ is the carrier frequency, $F(t)$ is the field amplitude, $\delta$ is the carrier-envelope phase and

$$\hat{\varepsilon}_\sigma^L = \frac{\hat{x}^L + \sigma i \hat{y}^L}{\sqrt{2}} \tag{6}$$

describes the pulse polarization. The excitation amplitudes are:

$$a_i(\varrho) = -i[R(\varrho)\hat{\varepsilon}_\sigma^L \cdot \mathbf{d}_{i,0}]\mathcal{E}(\omega_{i0}) \tag{7}$$

where $i=1,2$ labels the excited states, $\mathcal{E}(\omega_{i0})$ are the spectral amplitudes at the transition frequencies $\omega_{i0}$, $\mathbf{d}_{i,0}$ are the excitation dipole matrix elements in the molecular frame, and the pump field is rotated into the molecular frame via the rotation matrix $R(\varrho)$, with the Euler angles $\varrho \equiv (\alpha, \beta, \gamma)$ (see Supplementary Information for explicit expressions). The induced dipole in the molecular frame is:

$$\mathbf{d}_\varrho(\tau) = \sum_{i,j=0}^{2} a_i^*(\varrho)a_j(\varrho)e^{-i\omega_{ji}\tau}\mathbf{d}_{i,j} \tag{8}$$

where $\mathbf{d}_{i,j} = \langle i \mid \hat{\mathbf{d}} \mid j \rangle$ and $\omega_{ij} = \omega_i - \omega_j$. Transforming to the laboratory frame and averaging over all orientations $\varrho$ yields

$$\overline{\mathbf{d}}^L(\tau) = \int d\varrho R^t(\varrho)\mathbf{d}_\varrho(\tau) = \sum_{i,j=0}^{2} e^{-i\omega_{ji}\tau}\left\{\int d\varrho a_i^*(\varrho)a_j(\varrho)R^t(\varrho)\right\}\mathbf{d}_{i,j} \tag{9}$$

where $R^t = R^{-1}$ is the transpose of the rotation matrix $R$. Details of the integration are presented in the Supplementary Information. The final result is:

$$\overline{\mathbf{d}}^L = \frac{1}{3}\begin{pmatrix} \sqrt{2}\left[\mid \mathcal{E}(\omega_{10}) \mid (d_{1,0})^2 \cos\left(\omega_{10}\tau - \phi_1 - \frac{\pi}{2}\right) \right. \\ \left. + \mid \mathcal{E}(\omega_{20}) \mid (d_{2,0})^2 \cos\left(\omega_{20}\tau - \phi_2 - \frac{\pi}{2}\right)\right] \\ \sigma\sqrt{2}\left[\mid \mathcal{E}(\omega_{10}) \mid (d_{1,0})^2 \sin\left(\omega_{10}\tau - \phi_1 - \frac{\pi}{2}\right) \right. \\ \left. + \mid \mathcal{E}(\omega_{20}) \mid (d_{2,0})^2 \sin\left(\omega_{20}\tau - \phi_2 - \frac{\pi}{2}\right)\right] \\ \mid \mathcal{E}(\omega_{10}) \parallel \mathcal{E}(\omega_{20}) \mid \sigma[\mathbf{d}_{1,0} \times \mathbf{d}_{2,0}] \cdot \mathbf{d}_{1,2}\sin\left(\omega_{21}\tau - \phi_{21}\right) \end{pmatrix} \tag{10}$$

where $\mathcal{E}(\omega_{i0}) = \mid \mathcal{E}(\omega_{i0})\mid \exp\left(i\phi_i\right)$, $\phi_{21} = \phi_2 - \phi_1$. The $\pi/2$ phase shift reflects the resonance. Equation (1) shows the $z$ component, for $\phi_{21} = 0$. Note that $d_z^L$ is a time-even pseudo-scalar; that is, the quintessential chiral observable. Together with the $x$ and $y$ components, which describe rotation in the polarization plane, $d_z^L$ describes the helical charge motion induced in a randomly oriented chiral ensemble. The planar rotation stems from the coherence with the ground state, and the motion along the $z$ axis from the coherence between the excited states. The bound current is obtained by differentiating the dipole:

$$\overline{\mathbf{j}}^L = \frac{1}{3}\begin{pmatrix} -\sqrt{2}\left[\mid \mathcal{E}(\omega_{10}) \mid \omega_{10}(d_{1,0})^2 \sin\left(\omega_{10}\tau - \phi_1 - \frac{\pi}{2}\right) \right. \\ \left. + \mid \mathcal{E}(\omega_{20}) \mid \omega_{20}(d_{2,0})^2 \sin\left(\omega_{20}\tau - \phi_2 - \frac{\pi}{2}\right)\right] \\ \sigma\sqrt{2}\left[\mid \mathcal{E}(\omega_{10}) \mid \omega_{10}(d_{1,0})^2 \cos\left(\omega_{10}\tau - \phi_1 - \frac{\pi}{2}\right) \right. \\ \left. + \mid \mathcal{E}(\omega_{20}) \mid \omega_{20}(d_{2,0})^2 \cos\left(\omega_{20}\tau - \phi_2 - \frac{\pi}{2}\right)\right] \\ \mid \mathcal{E}(\omega_{10}) \parallel \mathcal{E}(\omega_{20}) \mid \omega_{21}\sigma[\mathbf{d}_{1,0} \times \mathbf{d}_{2,0}] \cdot \mathbf{d}_{1,2}\cos\left(\omega_{21}\tau - \phi_{21}\right) \end{pmatrix} \tag{11}$$

The strength of the chiral response in PXCD depends on the efficiency of conversion of the planar current excited by the pump field into the helical current

with the chiral component along the $z$ axis. The conversion is performed by the chiral molecule itself, see Supplementary Fig. 1.

**Probing chiral currents.** The photoelectron current in equation (3) is derived by applying the perturbation theory to the coherent excitation amplitudes calculated above. The ionizing probe field with frequency $\omega'$ is linearly polarized along the laboratory $\hat{x}^L$ axis and is delayed (delay $\tau$) from the pump field. The current for the photoelectron momentum $\vec{k}$ in the molecular frame is

$$\mathbf{J}(\mathbf{k}) = \frac{1}{2}a_\mathbf{k}^* a_\mathbf{k}\mathbf{k} + \text{c.c.} \tag{12}$$

where the population amplitude of the continuum state $\mid\mathbf{k}\rangle$ is (see Supplementary Information)

$$\begin{aligned} a_\mathbf{k} = &-(R(\varrho)\hat{\varepsilon}_\sigma^L \cdot \mathbf{d}_{1,0})(R(\varrho)\hat{x}^L \cdot \mathbf{D}_1)e^{-i\omega_1\tau}\mathcal{E}(\omega_1)\mathcal{E}'(\omega_{\mathbf{k}1}) \\ &-(R(\varrho)\hat{\varepsilon}_\sigma^L \cdot \mathbf{d}_{2,0})(R(\varrho)\hat{x}^L \cdot \mathbf{D}_2)e^{-i\omega_2\tau}\mathcal{E}(\omega_2)\mathcal{E}'(\omega_{\mathbf{k}2}) \end{aligned} \tag{13}$$

Here $\mathcal{E}'(\omega_{\mathbf{k},i})$ is the spectral amplitude of the probe at the required transition frequency, and $\mathbf{D}_i(\mathbf{k})$ are bound–free transition dipoles in the molecular frame.

The current includes both diagonal contributions and the Raman-type coupling of states $i = 1, 2$ via the continuum. Only the latter survives the orientation averaging (see Supplementary Information). Substituting expressions for the continuum amplitudes, and keeping only the off-diagonal terms, we obtain the current in the molecular frame:

$$\begin{aligned} \mathbf{J}(\mathbf{k},\varrho) = &(R(\varrho)\hat{\varepsilon}_{-\sigma}^L \cdot \mathbf{d}_{2,0}^*)(R(\varrho)\hat{x}^L \cdot \mathbf{D}_2^*)(R(\varrho)\hat{\varepsilon}_\sigma^L \cdot \mathbf{d}_{1,0})(R(\varrho)\hat{x}^L \cdot \mathbf{D}_1)\mathcal{E}(\omega,\omega')e^{i\omega_{21}\tau} \\ &\mathbf{k} + \text{c.c.} \end{aligned} \tag{14}$$

where $\mathcal{E}(\omega,\omega')$ includes all spectral amplitudes of the pump and probe pulses for the relevant transition frequencies,

$$\mathcal{E}(\omega,\omega') = \mathcal{E}^*(\omega_2)\mathcal{E}(\omega_1)\mathcal{E}'^*(\omega_{\mathbf{k}2}')\mathcal{E}'(\omega_{\mathbf{k}1}') \tag{15}$$

Note that $\mathbf{J}(\mathbf{k})$ is independent of the carrier-envelope phase $\delta$ of the pump. Hence, it also does not matter whether the probe is linearly polarized along the $x$ or the $y$ axis.

After transforming the current into the laboratory frame $\mathbf{J}^L(\mathbf{k},\varrho) = R^t(\varrho)\mathbf{J}$, averaging over all molecular orientations, and over all directions of $\mathbf{k}$ we obtain:

$$\overline{J}_z^L(k) = -\frac{\sigma}{60}\mathcal{E}(\omega,\omega')[\mathbf{d}_{1,0} \times \mathbf{d}_{2,0}] \cdot \mathbf{D}_{12}(k)e^{i\left(\omega_{21}\tau - \frac{\pi}{2}\right)} + \text{c.c.} \tag{16}$$

$$\overline{J}_x^L(k) = \overline{J}_y^L(k) = 0 \tag{17}$$

$$\mathbf{D}_{12}(k) = \int d\Omega_k \mathbf{D}_{12}(\mathbf{k}) \tag{18}$$

and the vector $\mathbf{D}_{12}(\mathbf{k})$ is defined below. Writing the Raman-type photoionization vector $\mathbf{D}_{12}(\mathbf{k})$ as a sum of its real and imaginary parts, we obtain equation (3), up to constant multipliers (omitted there for compactness):

$$\begin{aligned} \overline{J}_z^L(k) &= -\frac{\sigma}{60}\mid \mathcal{E}(\omega,\omega') \mid [\mathbf{d}_{1,0} \times \mathbf{d}_{2,0}] \\ &\quad \cdot (\mathbf{D}_{12}^r(k) + i\mathbf{D}_{12}^i(k))e^{i\left(\omega_{21}\tau + \phi(\omega,\omega') - \frac{\pi}{2}\right)} + \text{c.c.} \\ &= -\frac{\sigma}{30}\mid \mathcal{E}(\omega,\omega') \mid [\mathbf{d}_{1,0} \times \mathbf{d}_{2,0}] \cdot \\ &\quad \cdot [\mathbf{D}_{12}^r(k)\sin(\omega_{21}\tau + \phi(\omega,\omega')) \\ &\quad + \mathbf{D}_{12}^i(k)\cos(\omega_{21}\tau + \phi(\omega,\omega'))] \end{aligned} \tag{19}$$

Here the phases and amplitudes of the pump and probe fields are denoted $\phi(\omega,\omega')$ and $\mid\mathcal{E}(\omega,\omega')\mid$. The real part of the Raman-type photoionization dipole is equal to zero due to time-reversal symmetry of the set-up. For $\mathbf{D}_{12}(\mathbf{k})$, we find (see Supplementary Information)

$$\mathbf{D}_{12}(\mathbf{k}) = -4(\mathbf{D}_1 \cdot \mathbf{D}_2^*)\mathbf{k} + (\mathbf{D}_2^* \cdot \mathbf{k})\mathbf{D}_1 + (\mathbf{D}_1 \cdot \mathbf{k})\mathbf{D}_2^* \tag{20}$$

This general expression shows that every available vector $(\mathbf{D}_1, \mathbf{D}_2^*, \mathbf{k})$ can be used to 'complete' the triple product. We show below that the last two terms in this equation can be associated with partial alignment of the molecular ensemble by the pump pulse, and disappear if the unpolarized probe is used. However, the PXECD effect remains due to the first term in the above equation.

**PXECD for unpolarized probe pulse.** Theoretically, it is instructive to consider completely unpolarized light as a probe of the excited chiral dynamics. Since the probe is completely isotropic, it cannot be sensitive to the initial alignment by the pump. Thus, considering an unpolarized probe, we can find out how a partial alignment of the initially isotropic ensemble by the pump transition affects the chiral continuum current (the PXECD effect). Below, we show that the PXECD effect does not vanish if the alignment by the pump is excluded. Thus, the PXECD effect does not originate solely from a partial alignment by the pump pulse.

Consider an arbitrary direction of the linear probe in the laboratory frame. Instead of a single vector characterizing the direction of polarization $\hat{x}^L$ of the probe pulse, we introduce

$$\hat{p}^L = \begin{pmatrix} \sin\theta_p\cos\varphi_p \\ \sin\theta_p\sin\varphi_p \\ \cos\theta_p \end{pmatrix}$$

Then the current in equation (14) takes the form

$$\mathbf{J}(\mathbf{k},\varrho,\hat{p}^L) = \sum_{i,j} (R(\varrho)\hat{\varepsilon}^L_{-\sigma}\cdot\mathbf{d}_{2,0})\Big(R(\varrho)\hat{j}^{L*}\cdot\mathbf{D}^*_2\Big)$$
$$(R(\varrho)\hat{\varepsilon}^L_\sigma\cdot\mathbf{d}_{1,0})(R(\varrho)\hat{i}^L\cdot\mathbf{D}_1) \qquad (21)$$
$$p_i p_j^* \mathcal{E}(\omega,\omega')\mathbf{k}e^{i\omega_{21}\tau} + \text{c.c.}$$

where $i$ and $j$ take values $x, y, z$. From this expression, we can see that cross-terms $i \neq j$ vanish after averaging over probe-polarization directions; therefore, we need to calculate only the terms corresponding to a probe polarized along directions $\hat{x}^L$, $\hat{y}^L$ and $\hat{z}^L$ independently. We already calculated the expression for a probe polarized along $\hat{x}^L$ and demonstrated that it is valid for all probe polarizations in the $x^L y^L$ plane, and in particular for probe polarization along $\hat{y}^L$. For a probe polarized along $\hat{z}^L$, we obtain expressions identical to equations (16)–(19) for the current, except that $\mathbf{D}_{12}$ in equation (20) is now given by

$$\mathbf{D}_{12}(\mathbf{k},\hat{z}^L) = -2[(\mathbf{D}_1\cdot\mathbf{D}_2)\mathbf{k} + \mathbf{D}_1(\mathbf{D}^*_2\cdot\mathbf{k}) + \mathbf{D}^*_2(\mathbf{D}_1\cdot\mathbf{k})] \qquad (22)$$

From equations (20)–(22), the expression for the current in the laboratory frame reads as

$$\overline{J^L_z}(\mathbf{k},\hat{p}^L) = -\frac{\sigma}{60}\,|\,\mathcal{E}(\omega,\omega')\,|\,(\mathbf{d}_{1,0}\times\mathbf{d}_{2,0})\cdot\mathbf{D}_{12}(\mathbf{k};\hat{p}^L)$$
$$\times e^{i\left(\omega_{21}\tau - \frac{\pi}{2} + \phi(\omega,\omega')\right)} + \text{c.c.} \qquad (23)$$
$$+\text{cross}-\text{terms}$$

$$\mathbf{D}_{12}(\mathbf{k},\hat{p}^L) = \left(\Big[\,|\,p_x\,|^2 + |\,p_y\,|^2\Big]\mathbf{D}_{12}),\hat{x}^L) + |\,p_z\,|^2\,\mathbf{D}_{12}(\mathbf{k},\hat{z}^L)\right)$$
$$= -2\left[2-\left(\hat{n}^L\cdot\hat{p}^L\right)^2\right](\mathbf{D}_1\cdot\mathbf{D}^*_2)\mathbf{k} \qquad (24)$$
$$+\left[1-3\left(\hat{n}^L\cdot\hat{p}^L\right)^2\right][(\mathbf{D}^*_2\cdot\mathbf{k})\mathbf{D}_1 + (\mathbf{D}_1\cdot\mathbf{k})\mathbf{D}^*_2]$$

where $\hat{n}^L = \hat{z}^L$ is the propagation direction of the pump. The coefficient $\left[1-3\left(\hat{n}^L\cdot\hat{p}^L\right)^2\right]$ vanishes after averaging over orientations of the probe and we obtain the simple expression

$$\mathbf{D}^u_{12}(\mathbf{k}) = \int d\phi_p \int d\theta_p \sin\theta_p \mathbf{D}_{12}(\mathbf{k},\hat{p}^L)$$
$$= -\frac{10}{3}(\mathbf{D}_1\cdot\mathbf{D}^*_2)\mathbf{k} \qquad (25)$$

which, once integrated over orientations of $\mathbf{k}$ (see equation (18)), gives the Raman-type photoionization vector that goes into the final expression for the current in equation (19). Note that, once the partial alignment by the pump is excluded, only vector $\mathbf{k}$ can be used to 'complete' the triple product.

**PXECD in the plane-wave continuum.** So far, all of our calculations have been general. We now consider the case of the plane-wave continuum, eliminating any

possibility of chiral contributions from the continuum (that is, the photoelectron scattering from the chiral potential of the core). We write the photoionization dipoles in the velocity gauge,

$$\mathbf{D}_i = \langle\mathbf{k}\,|\,\hat{\mathbf{p}}\,|\,\psi_i\rangle = \mathbf{k}\widetilde{\psi_i}(\mathbf{k}), \qquad i=1,2 \qquad (26)$$

The photoionization matrix elements are proportional to the wavefunctions of the excited states in the momentum space, $\widetilde{\psi_i}(\mathbf{k})$. Putting these expressions in equation (20), we obtain

$$\mathbf{D}_{12}(\mathbf{k}) = -2k^2\widetilde{\psi_1}(\mathbf{k})\widetilde{\psi_2}^*(\mathbf{k})\mathbf{k} \qquad (27)$$

Thus, the Raman-type photoionization vector $\mathbf{D}_{12}(k) = \int d\Omega_k\mathbf{D}_{12}(\mathbf{k})$ becomes:

$$\mathbf{D}^{PW}_{12}(k) = -2\int d\Omega_k k^2\widetilde{\psi_1}(\mathbf{k})\widetilde{\psi_2}^*(\mathbf{k})\mathbf{k} \qquad (28)$$

We now show that $\mathbf{D}^{PW}_{12}(k)$ is purely imaginary. We split the electronic wavefunctions $\psi_{1,2}(\mathbf{r})$ of the bound states $|\,1\rangle$ and $|\,2\rangle$ in coordinate space into their symmetric and antisymmetric components:

$$\psi_{1,2}(\mathbf{r}) = \psi^S_{1,2}(\mathbf{r}) + \psi^A_{1,2}(\mathbf{r}) \qquad (29)$$

Their Fourier transforms are

$$\widetilde{\psi}_{1,2}(\mathbf{k}) \equiv \int d\mathbf{r}\psi_{1,2}(\mathbf{r})e^{i\mathbf{kr}} = \int d\mathbf{r}\psi^S_{1,2}(\mathbf{r})\cos(\mathbf{k}\cdot\mathbf{r})$$
$$+ i\int d\mathbf{r}\psi^A_{1,2}(\mathbf{r})\sin(\mathbf{k}\cdot\mathbf{r}) \qquad (30)$$
$$\equiv \widetilde{\psi}^S_{1,2}(\mathbf{k}) + i\widetilde{\psi}^A_{1,2}(\mathbf{k})$$

where both $\widetilde{\psi}^A_{1,2}(\mathbf{k})$ and $\widetilde{\psi}^S_{1,2}(\mathbf{k})$ are real functions. After simple algebra we get:

$$\mathbf{D}^{PW}_{12}(k) = 2i\int d\Omega_k k^2\Big(\widetilde{\psi}^S_1(\mathbf{k})\widetilde{\psi}^A_2(\mathbf{k}) - \widetilde{\psi}^A_1(\mathbf{k})\widetilde{\psi}^S_2(\mathbf{k})\Big)\mathbf{k} \qquad (31)$$

Thus, $\mathbf{D}^{PW}_{12}(k)$ is purely imaginary:

$$\mathbf{D}^{PW}_{12}(k) = i\mathbf{D}^{i,PW}_{12}(k) \qquad (32)$$

Taking into account equation (32) and using explicitly the imaginary component of the Raman-type photoionization vector $\mathbf{D}^{i,PW}_{12}(k)$, we obtain equation (4):

$$\overline{J^{L,PW}_z}(k) = -\frac{\sigma}{30}\frac{|\,\mathcal{E}(\omega,\omega')\,|}{\omega'_{k1}\omega'_{k2}}[\mathbf{d}_{1,0}\times\mathbf{d}_{2,0}]\cdot\mathbf{D}^{i,PW}_{12}(k)\cos(\omega_{21}\tau + \phi(\omega,\omega')) \qquad (33)$$

The constants as well as the phases and amplitudes of the pump and probe fields $\phi(\omega,\omega')$, and $|\,\mathcal{E}(\omega,\omega')\,|$ at the excitation and probe frequencies, appearing in equation (33), were omitted in equation (4) for compactness and clarity of our equations. Importantly, equation (33) shows that the PXECD current remains chiral for every $k$, even when the effects of chirality in the continuum are removed by using a plane-wave continuum. Thus, PXECD can be used as a probe exclusively sensitive to chiral bound dynamics.

We now establish the relationship between the PXECD current and the total PXECD current integrated over all $k$. First, we compare the Raman-type photoionization vector integrated over all $k$ ($d\mathbf{k} \equiv d\Omega_k k^2$):

$$-\frac{1}{2}\int d\mathbf{k}\mathbf{D}^{PW}_{12}(k) \equiv \int d\mathbf{k}\widetilde{\psi_1}(\mathbf{k})\widetilde{\psi_2}^*(\mathbf{k})\mathbf{k} \qquad (34)$$

and the bound transition dipole between the two excited states $\mathbf{d}_{1,2}$. This dipole can be written in a strikingly similar form:

$$i\omega_{21}\mathbf{d}_{1,2} \equiv \int d\mathbf{k}\widetilde{\psi_1}(\mathbf{k})\widetilde{\psi_2}^*(\mathbf{k})\mathbf{k} \qquad (35)$$

The right-hand sides of equations (34) and (35) are equivalent. Thus, $i\omega_{21}\mathbf{d}_{1,2}$ and $-\int d\mathbf{k}\mathbf{D}^{PW}_{12}(k)/2$ are also equivalent. If $\omega_{21} = 0$, the Raman-type photoionization vector integrated over all $k$ is also zero.

Thus, we recover a simple connection between the bound transition dipole $\mathbf{d}_{1,2}$ and the integrated Raman-type photoionization vector:

$$\omega_{21}\mathbf{d}_{1,2} \equiv -\frac{1}{2}\int dk\mathbf{D}^{i,PW}_{12}(k) \qquad (36)$$

Here we explicitly used that $\mathbf{D}^{PW}_{12}(k)$ is purely imaginary. This is evident from equations (32) and (35). Using this simple connection and integrating the

continuum current over all $k$ (assuming adjustable strength of the probe pulse at all frequencies, so that $C_\mathcal{E} = \frac{1}{5}\frac{\mathcal{E}'^*(\omega'_{k2})\mathcal{E}(\omega'_{k1})}{\omega'_{k1}\omega'_{k2}}$ is independent of $k$), we obtain a simple relationship between the bound and total (integrated over all $k$) continuum currents:

$$J_{tot}^{PXECD} \equiv \int dk\, \overline{J_z^{L,PW}}(k) \tag{37}$$

$$J_{tot}^{PXECD} = C_\mathcal{E} j_z^{PXCD} \tag{38}$$

Here we used equations (11), (33) and (36). Despite its simplicity, equation (38) is important for understanding the PXECD phenomenon. It shows that even if one explicitly removes the effects associated with the chirality of the molecular continuum or effects associated with the non-spherical symmetry of the molecular continuum (by using a plane-wave continuum instead), the PXECD current remains chiral, not only for every $k$ (see equation (33)), but also integrally for all $k$, because in this case it directly reflects the chirality of the bound PXCD current. If the bound current is equal to zero (for example, when the two bound states are degenerate), then the total continuum current is also equal to zero.

**The nature of the PXECD current.** We can now address the question about the mechanisms leading to the PXECD current more broadly. The PXECD continuum current may arise due to the following reasons: due to bound PXCD current; due to partial alignment of the molecular ensemble by the pump pulse; or due to the degenerate PXECD process, even in the absence of bound PXCD current (that is, when $\omega_{12} = 0$). Degenerate PXECD is the PXECD for degenerate excited states.

Equation (19) is general; it contains all three effects. The set of examples that we have considered in previous subsections allows us to identify and to isolate each of these effects. The effect of partial alignment due to the pump pulse can be 'removed' by considering an unpolarized probe. Equation (25) shows that the chiral response does not vanish in this case. Finally, to isolate the degenerate PXECD process, one can remove the first two effects by considering unpolarized light and setting $\omega_{12} = 0$. When these effects are removed, for $\omega_{12} = 0$ and an unpolarized probe:

$$\mathbf{D}_{12}^u(\mathbf{k}) = -\frac{10}{3}(\mathbf{D}_1(\mathbf{k}) \cdot \mathbf{D}_2^*(\mathbf{k}))\mathbf{k} \tag{39}$$

and the PXECD current is:

$$\overline{J_z^\perp}(k) = \frac{\sigma}{9} \mid \mathcal{E}(\omega, \omega') \mid \int d\Omega_k [\mathbf{d}_{1,0} \times \mathbf{d}_{2,0}] \cdot \mathbf{k}(\mathbf{D}_1^i(\mathbf{k}) \cdot \mathbf{D}_2^r(\mathbf{k}) - \mathbf{D}_1^r(\mathbf{k}) \cdot \mathbf{D}_2^i(\mathbf{k})) \tag{40}$$

In this expression, for simplicity we set the phases $\phi(\omega, \omega') = 0$.

In the previous subsection we have demonstrated that in the case of a plane-wave continuum, the total PXECD current (integrated over all $k$) vanishes if we set $\omega_{12} = 0$. However, each momentum component of this current remains finite as long as the excited states $|1\rangle$ and $|2\rangle$ do not have definite parity, and $d_{12} \neq 0$. Note that the triple product in equation (40) is formed by the two bound dipoles and the vector $\mathbf{k}$ of the continuum electron.

**Inverse Abel transform of the two-photon chiral signal.** Here we show how the Abel-inverted quantities $\alpha$ and $\alpha'$ (Fig. 4) are connected to the conventional asymmetry parameters of the three-dimensional (3D) photoelectron signal.

Experimentally, the photoelectron spectrum closely follows the spectrum of the probe: the spectra are located within a bell-shaped 3D sphere $G_0(k, k_0)$, where

$E_0 = k_0^2/2$ is the central energy, with width $\Delta E \ll E_0$. In the geometry of our experiment, the 3D chiral asymmetry signal can be written as

$$R_{3D}^{PXECD} = CG_0(k, k_0)$$
$$\times \Big[ q_{1,0}P_1^0(\cos\theta) + q_{2,-2}P_2^2(\cos\theta)\sin(2\phi) + q_{3,0}P_3^0(\cos\theta) \tag{41}$$
$$+ q_{3,2}P_3^2(\cos\theta)\cos(2\phi)\Big]$$

where $C$ depends on the gas density and so on. The Legendre polynomials $P_2^2$ and $P_3^2$ reflect the geometry of the experiment, where the pump field is propagating along the $z$ axis. The parameters $q_{2,-2}$ and $q_{32}$ appear due to the breaking of the cylindrical symmetry in our experimental set-up; $q_{32}$ reflects the chiral asymmetry, changing sign with changing light helicity or enantiomer handedness. The 3D signal is projected onto the 2D $x$–$z$ plane, simulating the measurement, and then raised back to 3D, simulating the reconstruction. The modelling is done numerically using the experimentally measured $G_0(k, k_0)$. The analytical model will be described elsewhere. The presence of $q_{32}$ modifies the reconstructed 3D image in two ways. First, $\alpha$ and $\alpha'$ (Fig. 4) contain $q_{32}$: $\alpha = q_{10} + 6q_{32}$ and $\alpha' = q_{10} - 6q_{32}$. Secondly, a characteristic signal $\propto q_{32}(k/k_0)P_1^0(\cos\theta)$ for $k < k_0$ lying outside the spectral bandwidth of the pulse may appear as a signature of $q_{32}$. This background allows us to give the upper estimate to $q_{32}$ from the 3D images directly obtained via the inverse Abel transform of the measured 2D spectra (see Supplementary Information).

**Numerical simulations.** The numerical results for PXCD and PXECD in fenchone, presented in Figs. 2 and 4, have been obtained using perturbative quantum-mechanical calculations that mimic the experimental pump–probe set-up. These calculations employ bound and continuum configuration-interaction single states in the framework of frozen nuclei and single-active electron approximations. Our simulations have shown that molecular chiral Rydberg wavepackets can be formed by absorption of a circularly polarized photon. In addition: the population of this wavepacket does not depend on the helicity within the dipole approximation; this wavepacket is inherently chiral, as imaged by the photoexcitation circular dichroism that survives orientation averaging within a set of randomly aligned targets as long as there is an electronic coherence between the excited states; when a linearly polarized probe is switched on, this chiral dichroism is transferred into the continuum and mapped onto the (usual) photoelectron circular dichroism, even in the plane-wave approximation; the electronic beating between the underlying wavepacket states is noticeable in the excitation and the related ionization dichroisms, as function of the pump–probe delay, but the beating is blurred in the total photoionization signal. All of this sheds new light on the origin of chirality, whose signature is no more constrained to molecular ionization but extends to the whole electronic spectrum, within the usual and intuitive dipole approximation. Extended details regarding the simulations are given in Supplementary Section III.

**Vibrational coherence in PXECD.** In Supplementary Section V, we discuss the role that the excitation of the vibrational wavepackets plays in PXECD. Our analytical results presented above are general and can be applied to both electronic and vibrational (vibronic) states. However, the non-collinearity of the excitation dipoles required in PXCD leads to the following conditions for observing vibrational PXECD. First, it requires the breakdown of the Franck–Condon approximation. This is expected to be the case for large molecules exhibiting broad vibrational lines. Indeed, the essence of this approximation is that the vibrational wavefunctions are sufficiently compact in coordinate space, so that the electronic transition dipoles do not change as a function of the vibrational coordinates within this compact region. If, however, the vibrational wavefunctions spread over considerable distances, the breakdown of the Franck–Condon approximation is expected and natural. Second, it requires multidimensional, at least 2D, potential energy surfaces, which is certainly the case for chiral molecules.

**Data availability.** The data that support the plots within this paper and other findings of this study are available from the corresponding author upon reasonable request.